Corrosion Science 100 (2015) 651–662

Contents lists available at ScienceDirect

Corrosion Science

journal homepage: www.elsevier.com/locate/corsci

Effects of alloyed Si on the autoclave corrosion performance and periodic corrosion kinetics in Zr–Sn–Nb–Fe–O alloys

Liangyu Chen[a,d], Jiuxiao Li[a], Yao Zhang[a], Lai-Chang Zhang[b], Weijie Lu[a,*], Lefu Zhang[c], Liqiang Wang[a,*], Di Zhang[a]

[a] State Key Laboratory of Metal Matrix Composites, Shanghai Jiao Tong University, Shanghai 200240, China
[b] School of Engineering, Edith Cowan University, 270 Joondalup Drive, Joondalup, Perth, WA 6027, Australia
[c] School of Nuclear Science and Engineering, Shanghai Jiao Tong University, Shanghai 200240, China
[d] School of Material Science and Engineering, Jiangsu University of Science and Technology, Zhenjiang, Jiangsu 212003, China

ARTICLE INFO

Article history:
Received 10 April 2015
Received in revised form 28 August 2015
Accepted 29 August 2015
Available online 1 September 2015

Keywords:
A. Zirconium
B. SEM
B. TEM
B. XRD
C. High temperature corrosion
C. Oxidation

ABSTRACT

This paper investigates the effect of alloyed Si on the autoclave corrosion performance and corrosion mechanisms of Zr–Sn–Nb–Fe–O alloys. Quantitative analyses are performed on the microstructure of alloys and their oxide behavior. The Si-containing alloy possesses improved corrosion resistance. The reason is that a trace of Si enhances the strength of alloy and thus slows the evolution of undulated interface of oxide/metal which is associated with the formation of cracks in the oxide. The generation of cracks is discussed in further detail in relation to corrosion kinetics. This work advances the understanding of improving the corrosion resistance of zirconium alloys.

1. Introduction

Zirconium alloys have been used in nuclear power industry for many years as fuel cladding tubes because of their low neutron absorption rate and proper corrosion resistance [1–8]. Corrosion of zirconium alloys is one of the main factors for the degradation of the zirconium alloy tubes in service. According to previous studies, corrosion behavior initially takes place at the surface of zirconium alloys resulting in the form of oxide, then the oxide/metal interface moves towards matrix inside by inward diffusion of oxygen ions [4,7]. The weight gain of zirconium alloy is mainly obedient to cubic or parabolic law [7]. Generally, once the oxide has reached a few microns in thickness (pre-transition), an acceleration of corrosion kinetics is observed (post-transition), followed by a second cycle of parabolic/cubic growth rate [7].

The oxide growth produces a large change in volumes between metal and oxide, accompanied with large compressive stress in the oxide [9,10], which must be balanced by tensile stress in metal substrate [11]. Therefore, even a small increase in the size of in-plane oxide leads to high compressive stress which gives rise to the formation of undulations of oxide/metal interface [12]. It has been previously reported that the undulations promoting cracks formation in the oxide are correlated to the corrosion kinetic transition [4,13].

There exist some factors that play important roles in the nucleation of cracks, such as second phase particles (SPPs) and the transformation from tetragonal (t) to monoclinic (m) phase of ZrO_2 [14–18]. Compared to the surrounding matrix, the lower corrosion rate of SPPs leads to the formation of voids and cracks between SPPs and oxide [14,15]. However, other viewpoints supported by additional stress build-up induced by volume dilation of oxidized SPPs is susceptible to the formation of cracks [16,17]. On the other hand, the transformation of t → m is associated with 5% volume dilation, leading to the formation of cracks [17,18].

The properties of zirconium alloys depend basically on their chemical compositions [19–22]. As alloying elements may have adverse effects on corrosion resistance, it is prudent to select appropriate alloying element to improve the corrosion resistance of zirconium alloys. Si possesses a good semi-conductive characteristic and low thermal neutron absorption cross-section [23,24]. The oxidation valence of Si ion is +4 and equal to the valence of the Zr ion in ZrO_2. According to Hauffe–Wagner theory [25], Si^{4+} could keep the local electrical neutrality in oxide and would not produce

* Corresponding authors. Fax: +86 21 34202749.
E-mail addresses: luweijie@sjtu.edu.cn (W. Lu), wang_liqiang@sjtu.edu.cn (L. Wang).

http://dx.doi.org/10.1016/j.corsci.2015.08.043
0010-938X/

Table 1
Chemical composition (in wt.%) of the materials.

Alloy	Alloying elements					
	Zr	Sn	Fe	Nb	Si	O
ZrNbFeO	Balance	0.54	0.32	0.41	–	0.081
ZrNbFeSiO	Balance	0.51	0.33	0.40	0.021	0.079

oxygen vacancies. Moreover, from the Zr–Si phase diagram, the solubility of Si in α- or β-Zr is considerably low [26]. Si would easily precipitate in the form of SPPs in zirconium alloys, even if a trace of Si is added to zirconium alloys.

Our previous study showed that the Si-containing Zr–Sn–Nb–Fe–O alloys exhibited proper corrosion resistance [27]. In order to clarify the effect of alloyed Si on the corrosion performance of Zr–Sn–Nb–Fe–O alloy, the corrosion performance of a Si-free sample is also presented for comparison purpose. To assess the corrosion resistance of the experimental alloys, autoclave tests were conducted up to 200 days. Weight gain changes were observed as a measure of corrosion resistance. Meanwhile, the microstructure, second phase particle type, oxide cross-sectional microstructure, and the fraction of tetragonal phase were characterized in detail. The evolution of oxide, such as the undulations at the interface, cracks within oxide, the grain morphology and the phase constitution during corrosion, was also investigated to understand the corrosion mechanism and to build the correlation of alloyed Si and corrosion properties.

2. Experimental

2.1. Materials preparation

Zr–Sn–Nb–Fe–O (denoted as ZrNbFeO hereafter) and Zr–Sn–Nb–Fe–Si–O (denoted as ZrNbFeSiO hereafter) alloys were prepared by a sequence of three vacuum arc re-melting to obtain chemical homogeneity. Sn, Nb, Fe, Si powders with high purity (greater than 99.9%) were added. The chemical composition of the alloys is shown in Table 1. The as-prepared disk-shape ingots were 50 mm in thickness and 120 mm in diameter. After forged at 1000 °C, the thickness of ingots was reduced to 10 mm, followed by β-quenching. Thereafter, samples were prepared by conventional method and hot rolled to 3 mm at 600 °C, annealed at 570 °C for 1 h, followed by cold rolling to 0.6 mm thick plates with 2 intermediate heat treatments at 570 °C for 1 h. After final cold rolling, samples were annealed at 570 °C for 5 h.

2.2. Autoclave corrosion

Samples used for autoclave corrosion testing were 15 mm × 20 mm in size and chemically polished using a pickling solution (H_2O:HNO_3:H_2SO_4:HF = 3:3:3:1) at 30–50 °C and finally cleaned by deionized water. The concentration of HNO_3, H_2SO_4 and HF was 68%, 98% and 40%, respectively. The corrosion resistance of the samples was evaluated by measuring their weight gain per unit surface area in relation to the exposure time such as 3, 7, 14, 42, 70, 100, 130, 160, and 200 days. Corrosion experiments were conducted with a static isothermal autoclave in both deionized water and 0.01 mol/L LiOH aqueous solution at 360 °C under a saturation pressure of 18.6 MPa, respectively.

2.3. Microstructure characterization of alloys and oxide cross-sectional samples

The microstructures of the samples were characterized using a FEI Sirion 200 field emission gun scanning electron microscope (SEM) and a JEOL-2100F transmission electron microscope (TEM) equipped with an energy dispersive X-ray spectroscopy (EDS) detector with an accelerated voltage of 200 kV.

The samples for SEM observations were polished according to standard metallographic techniques and then etched in a hybrid solution (H_2O:HNO_3:HF = 9:9:2). A gold layer sputtered to the oxide cross-sectional samples was used to improve the surface conductivity of the oxide cross-sectional samples, preventing the accumulation of electrostatic charge, thereby minimizing image artifacts. The alloy samples for TEM observations were prepared using a twin-jet polishing with a solution (C_2H_5OH:$HClO_4$ = 9:1) at a voltage of 20 V and a temperature of −30 °C. The concentration of C_2H_5OH and $HClO_4$ was 99.7% and 72%, respectively. The oxide cross-sectional samples for TEM observations were prepared according to the following procedures. Transverse cross-sectional segments of about 1 mm width were cut from the corroded samples. The outer oxide was placed next to the outer one from another slice. The samples were then inserted directly into a titanium tube of 3 mm diameter and fixed in place with epoxy. Slices with a thickness of ~0.5 mm were then cut from the titanium tube to provide several 3-mm-diameter disks with the oxide cross-section located near the center of the disk. The disk samples were polished using 4000 grits SiC paper on both sides until the thickness reached to ~40 μm. The final thinning was performed using a Gatan Model 691 PIPS (Precision Ion Polishing System) instrument. The crystallographic characteristics of oxide grains were determined by high resolution TEM (HRTEM) using Image-Pro Plus 5.0.

2.4. Tensile tests

Tensile tests were performed using a Zwick Z100/SN3A universal testing machine at both room temperature and 380 °C (the usually working temperature is 280–300 °C [5,6]). Dog-bone flat tensile samples with a nominal gauge length of 15 mm and a cross-section of 12 mm × 0.6 mm were cut by electric discharge machining from the final samples parallel to the rolling direction. The samples were subsequently mechanically ground with 2000 grit SiC paper. A displacement rate of 1 mm/min was used for all the tests.

2.5. X-ray diffraction analysis for t-ZrO_2 phase fraction

A Rigaku D/Max 2550 X-ray diffractometer (XRD) was used with Cu-Kα radiation. The XRD results (not shown here) indicated that phase constituents of the autoclave tested sample are α-Zr, m-ZrO_2 and t-ZrO_2. In the XRD analysis with phase identification, the volume ratio of the tetragonal to monoclinic phase was quantified by using the Garvie–Nicholson equation [28]:

$$\text{Tetragonal phase fraction} = \frac{I_{(101)t}}{I_{(101)t} + I_{(111)m} + I_{(\bar{1}11)m}} \quad (1)$$

3. Results

3.1. Autoclave corrosion

Fig. 1 shows the corrosion kinetics of the autoclave tested ZrNbFeO and ZrNbFeSiO samples as corrosion weight gain against autoclave exposure time. In deionized water, ZrNbFeO exhibits typical corrosion kinetics with an indication of change from pre- to post-transition at around 160 days (Fig. 1a). With up to 200 days (Fig. 1b), ZrNbFeSiO shows no apparent sign of a transition in corrosion kinetics. In LiOH aqueous solution, the post-transition phenomenon of ZrNbFeO (100 days) is also earlier than that of ZrNbFeSiO (160 days) as shown in Fig. 1c and d. The corrosion results indicate that a trace of Si substantially extend the

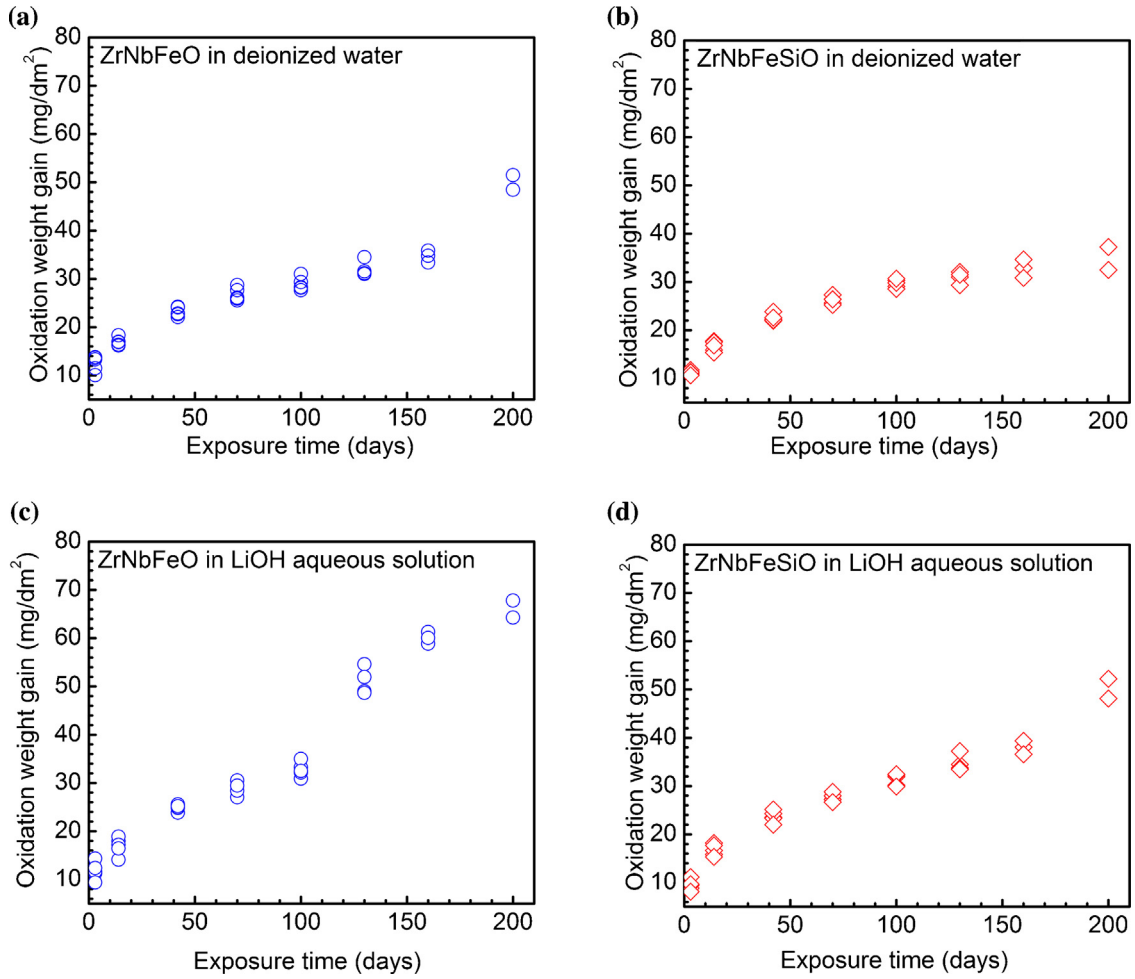

Fig. 1. Autoclave corrosion weight gain profile after 200 days at 360 °C/18.6 MPa for (a) ZrNbFeO, (b) ZrNbFeSiO in deionized water, (c) ZrNbFeO and (d) ZrNbFeSi in 0.01 mol/L LiOH aqueous solution.

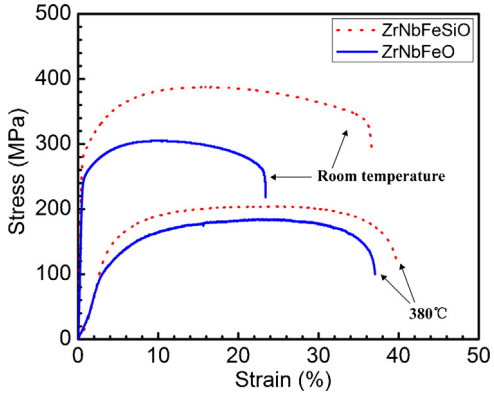

Fig. 2. Stress–strain curves for ZrNbFeO and ZrNbFeSiO at room temperature and at 380 °C. A trace of Si could effectively enhance the mechanical properties at both conditions.

pre-transition period of the Zr–Nb–Fe alloy in both corrosion conditions.

3.2. Tensile test results

Fig. 2 shows the stress-strain curves of ZrNbFeO and ZrNbFeSiO at both room temperature and 380 °C. It is interesting to note that a trace of Si has significantly enhanced both the strength and ductility of the ZrNbFeO alloy. The yield strength and ultimate tensile strength of ZrNbFeO are about 243 MPa and 305 MPa at room temperature and 95 MPa and 183 MPa at 380 °C, respectively. The elongations of ZrNbFeO are 23.4% and 37.1% at room temperature and 380 °C, respectively. After addition of 200 ppm Si, the yield strength and ultimate tensile strength have been increased to 286 MPa and 388 MPa respectively at room temperature and to 119 MPa and 204 MPa respectively at 380 °C. The elongations of ZrNbFeSiO have also been increased at both room temperature (36.6%) and 380 °C (39.7%).

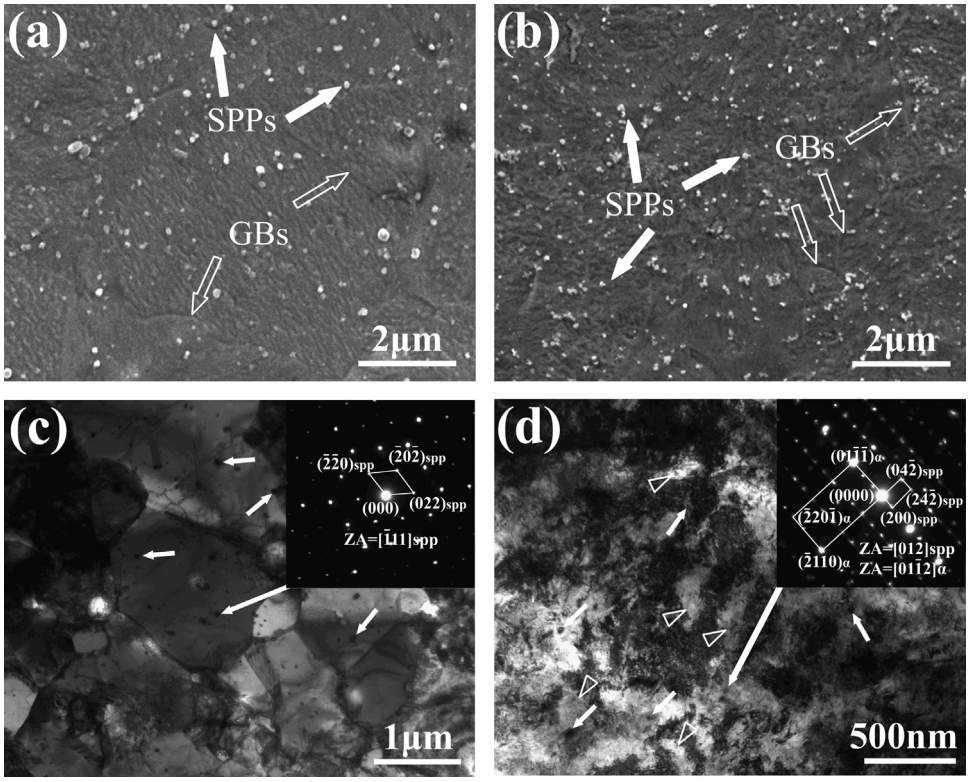

Fig. 3. SEM micrographs of (a) ZrNbFeO, (b) ZrNbFeSiO alloys and TEM micrographs of the typical microstructure for (c) ZrNbFeO and (b) ZrNbFeSiO alloys. The inset shows the selected area electron diffraction pattern of the particles indicated by the long arrows. Note: The white solid arrows indicate second phase particles (SPPs), the white hollow arrows indicate grain boundaries (GBs) and the white hollow triangles indicate dislocation cells.

3.3. Microstructural features

The microstructures of matrix and distribution of SPPs for the ZrNbFeO and ZrNbFeSiO alloys are revealed in Fig. 3. For the ZrNbFeO alloy (Fig. 3a), the grain boundaries (GBs) of the alloy are clearly observed, as indicated by white hollow arrows. Precipitates (as indicated by white solid arrows) are randomly distributed within the grains and along grain boundaries. In contrast, as seen from Fig. 3b, although the grain boundaries of ZrNbFeSiO are detected somewhere, no perfect grain could be resolved. The morphology of microstructure of ZrNbFeSiO indicates that equilibrium recrystallization is not yet reached. The SPPs of ZrNbFeSiO are randomly distributed as well as those of ZrNbFeO, but the SPPs in ZrNbFeSiO are finer than the ones in ZrNbFeO. Statistical data from SEM observations for SPPs are summarized in Table 2. It can be found the mean size of SPPs in ZrNbFeSiO (55 nm) is much smaller than that in ZrNbFeO (71 nm).

Fig. 3c and d presents the TEM image of typical microstructures for the ZrNbFeO and ZrNbFeSiO alloys. The typical recrystallized grains of ZrNbFeO alloy have relatively clean interiors with some SPPs randomly distributing in spherical or ellipsoidal morphology (Fig. 3c). Selected area electron diffraction of the SPPs in ZrNbFeO (the inset of Fig. 3c) indicates that the precipitate is $(Zr,Nb)_2Fe$ with a face-centered cubic (FCC) structure. As seen from the typical microstructure of ZrNbFeSiO in Fig. 3d, the addition of Si considerably increases the dislocation density and some dislocation cells are observed. In our previous study [27], sub-grains with grain size about 200 nm are found in the ZrNbFeSiO. It is speculated that these sub-grains are evolved from the dislocation cells as observed in Fig. 3d. In ZrNbFeSiO, the SPPs are also identified to be (Zr, Nb, $Si)_2Fe$ with FCC structure and containing at most ~2.0 wt.% Si.

3.4. Cross-sectional microstructure of oxide and the cracks of oxide

Fig. 4 exhibits the cross-sectional microstructure of the oxide at 100 days and 160 days in LiOH aqueous solution and the curves replicated from a segment of the interface of oxide/metal. It is evident that the 100 days and 160 days exposure time are critical points of from pre- to post-transition for ZrNbFeO and ZrNbFeSiO in LiOH aqueous solution, respectively (Fig. 1c and d). Before the transition of corrosion (100 days of exposure), a continuous oxide layer (~2 μm) has been observed for both alloys (Fig. 4a and b). A few cracks and undulated interface of oxide/metal are observed for ZrNbFeO (Fig. 4a). It is noted that the cracks are visible in specific regions, i.e. above the sharp undulations, which is also observed in other zirconium alloys [4,14,29,30]. In contrast, almost no crack is visible in the oxide in ZrNbFeSiO alloy (Fig. 4b) and the undulations of the interface have relatively smaller amplitudes when compared to those in ZrNbFeO (Fig. 4a).

When the exposure time was increased to up to 160 days, the thickness of the oxide in ZrNbFeO increased to ~4 μm (Fig. 4c). A

Table 2
Some statistical data from SEM observations for second phase particles in ZrNbFeO and ZrNbFeSiO alloys.

Alloy	Type	Structure	Nb + Fe + Si (wt.%)	Mean diameters (nm)	Volume fraction (%)
ZrNbFeO	$(Zr, Nb)_2Fe$	FCC	0.738	71	3.29
ZrNbFeSiO	$(Zr, Nb,Si)_2Fe$	FCC	0.754	55	3.23

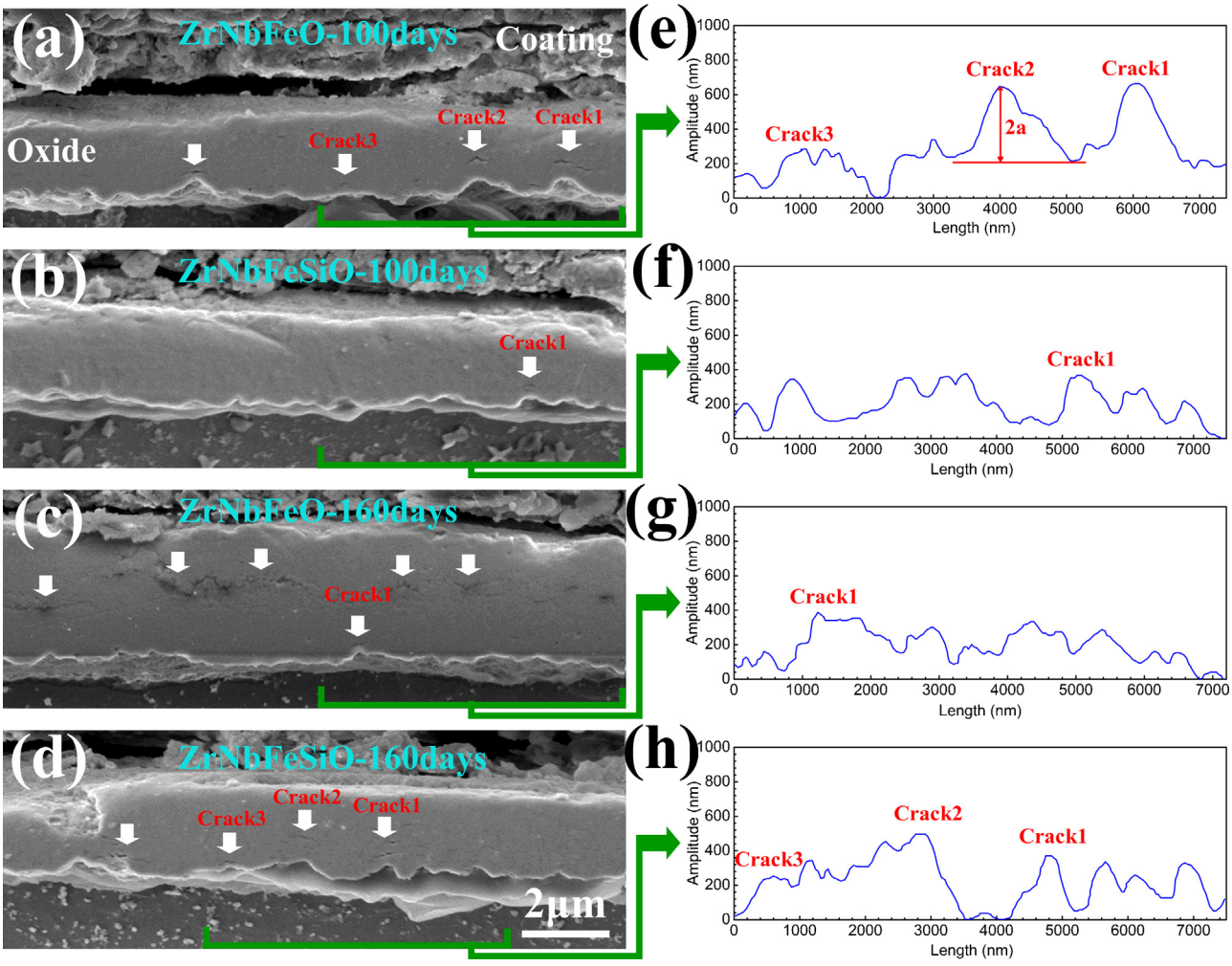

Fig. 4. SEM micrographs representative of the oxide (cross-section) in LiOH aqueous solution condition: (a) ZrNbFeO after 100 days exposure, (b) ZrNbFeSiO after 100 days exposure, (c) ZrNbFeO after 160 days exposure and (d) ZrNbFeSiO after 160 days exposure. The curves in (e)–(h) are replicated from a segment of the interface of oxide/metal as indicated by green square brackets. (For interpretation of the references to color in this figure legend, the reader is referred to the web version of this article.)

high density of cracks is also observed. The depth of these large cracks shown in Fig. 4c is in good agreement with the oxide thickness at which small cracks are observed in the thinner oxide sample (Fig. 4a), indicating that the small cracks are correlated to the corrosion proceeding. The large cracks obviously define the existence of two layers within the oxide. However, the undulations of interface at 160 days are milder than that at 100 days, indicating that the amplitude of undulations does not increase monotonously with the exposure time. As seen from Fig. 4d, a few cracks are found beyond the crest of undulations in ZrNbFeSiO and the undulations become sharper than those at 100 days (Fig. 4b). It seems that the undulations of ZrNbFeSiO have a slower evolution than those of ZrNbFeO.

The profiles of segments of interfaces were transformed into curves for easy analysis in coordinate axes as represented in Fig. 4e–h. As such, the amplitude of undulations which are associated with cracks could be measured, including the length of these cracks, as listed in Table 3. The linked-up large cracks in Fig. 4c are neglected in the examination. Since the undulations are produced by the deformation of matrix which caused by the stress in the oxide [13]. Then, stress can be relieved by cracking [30]. Large cracks are connected in the oxide and the oxide splits into two layers. The stress in outer layer oxide is rather low as far away from the interface [30]. Therefore, the interaction of outer layer oxide and matrix become minimal. It is expected that the main effect

Table 3
The amplitude of undulations associating with cracks and the length of these cracks.

Alloy	Exposure time (days)	Amplitude/length (nm)			The maximum amplitude (nm)
		Cracks 1	Cracks 2	Cracks 3	
ZrNbFeO	100	244/495	210/521	114/224	244
	160	170/316	–	–	170
ZrNbFeSiO	100	145/264	–	–	145
	160	115/224	297/435	184/462	297

of stress on matrix results from inner layer oxide. The minimum amplitude of undulations associating with crack is 115 nm in all measured cracks. As the amplitude increases, cracks propagate. The maximum amplitude of undulations reduces from 244 nm at 100 days to 170 nm at 160 days accompanying with few crack in the inner oxide layer in the case of ZrNbFeO (Fig. 4e and g). In ZrNbFeSiO, the maximum value of amplitude soars to 297 nm at 160 days from 148 nm at 100 days (Fig. 4f and h). Such trend in undulations with corrosion time before and after the transition has also been reported by other researchers, but without consensus [4,14].

Fig. 5 exhibits the relationship between the amplitude of undulations and the length of cracks. In order to ensure the reliability, along with the data in Table 3, more information of cracks was collected from other figures by using the same method mentioned

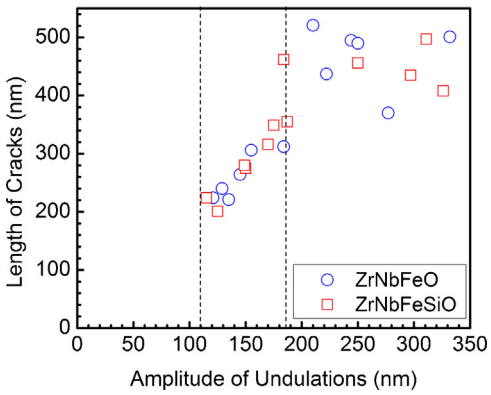

Fig. 5. Relationship between the length of cracks and the amplitude of undulations.

above. It is easily found that both alloys have identical behavior in cracks and three regions are clearly revealed in Fig. 5. Firstly, no apparently visible crack is observed in the region where the amplitude is less than 109 nm. Secondly, the length of cracks shows an approximate linear relationship with the amplitude of undulations when the amplitudes range from about 109 to 184 nm, indicating that sharper undulations are associated with higher tensile stress which is perpendicular to interface. The cracks are in the stable propagation stage [31]. Thirdly, the length of cracks represents an irregular value when the amplitude is greater than about 184 nm, whilst the lengths of cracks in this region are greater than those in the previous region. Crack growth gets into instable propagation [31].

3.5. Grain morphology and crystal structure of oxides

Fig. 6 reveals the grain morphology of oxide near the interface of ZrNbFeO and ZrNbFeSiO at 100 days exposure in LiOH aqueous. Oxide columnar grains in ZrNbFeO (Fig. 6a) and ZrNbFeSiO (Fig. 6b) grow in the direction perpendicular to the interface of oxide/metal and aligned tightly. As shown in Fig. 6c, the domains A–C are confirmed as tetragonal zirconia, monoclinic zirconia and monoclinic zirconia. In Fig. 6d, the domains D–F are confirmed as tetragonal zirconia, monoclinic zirconia and α-Zr. As lattice misfit exists between tetragonal grain A and monoclinic grain B, a semi-coherent grain boundary is formed as indicated by white triangles in Fig. 6c. Such lattice misfit is also observed between tetragonal grain D and monoclinic grain E as indicated in Fig. 6d. In Fig. 6d, a parallel orientation between the monoclinic phase and α-Zr, i.e. $(11\bar{1})_m // (11\bar{2}0)_\alpha$, is detected with almost no deviation. Moreover, the (110) or $(\bar{1}10)$ planes of tetragonal oxide grains and $(\bar{1}11)$ or (111) planes of monoclinic oxide grains are nearly parallel to (0001) in α-Zr with several degrees deviation.

Fig. 7 displays the equiaxed grains in the outer oxide layer of alloys at 100 days of exposure in LiOH aqueous solution. A large number of pores with nano-scale are formed at grain boundaries, as indicated by white arrows (Fig. 7a and b). It is speculated that the oxide is nearly transparent to the oxidizing species due to the short-cut effect of pores [32]. Both alloys show similar grain morphology of outer oxide layer in spite of different inner oxide layers (including undulations and cracks). Fig. 7c and d shows equiaxed grains all identified as monoclinic symmetry with large-sized pores lying on the grain boundary. No tetragonal phase and specific parallel orientation of monoclinic phase are observed near the pores.

Fig. 8 shows the SPPs incorporated in the oxide of alloys at 100 days of exposure in LiOH aqueous. The SPPs are about 0.5 μm from the oxide/metal interface and their chemical compositions are

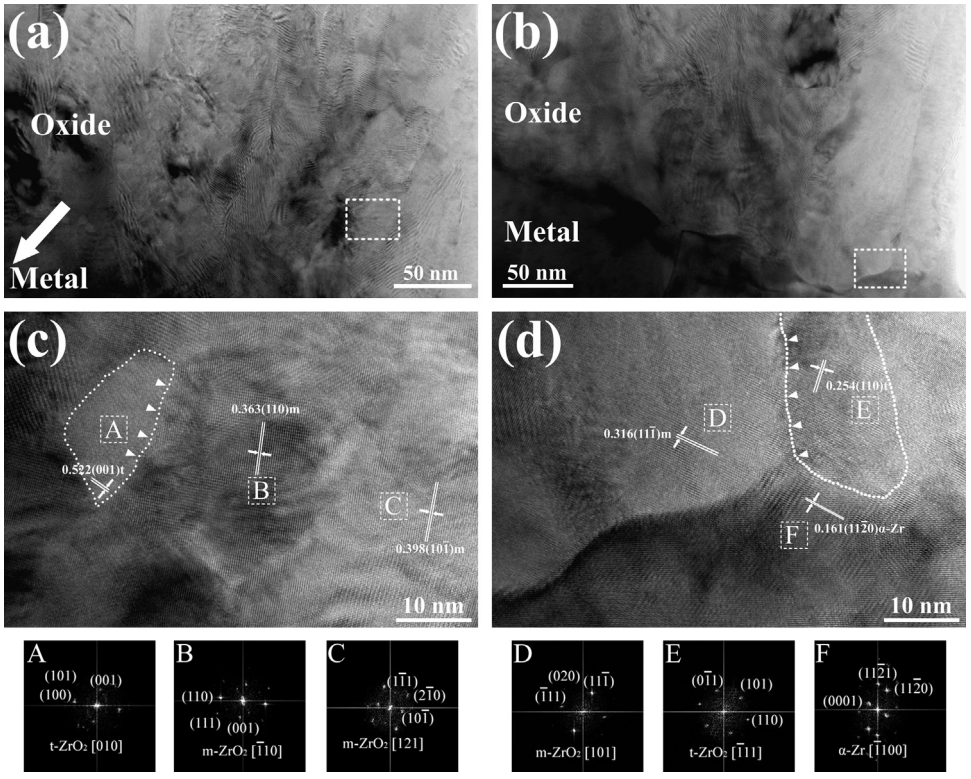

Fig. 6. TEM bright field micrographs of the regions near the oxide/metal interface for: (a) ZrNbFeO and (b) ZrNbFeSiO at 100 days of exposure in LiOH aqueous. (c) and (d) HRTEM images for the square region marked in (a) and (b), respectively. The Fast Fourier Transform (FFT) diffraction patterns in the bottom are for the square regions A–F marked in (c) and (d).

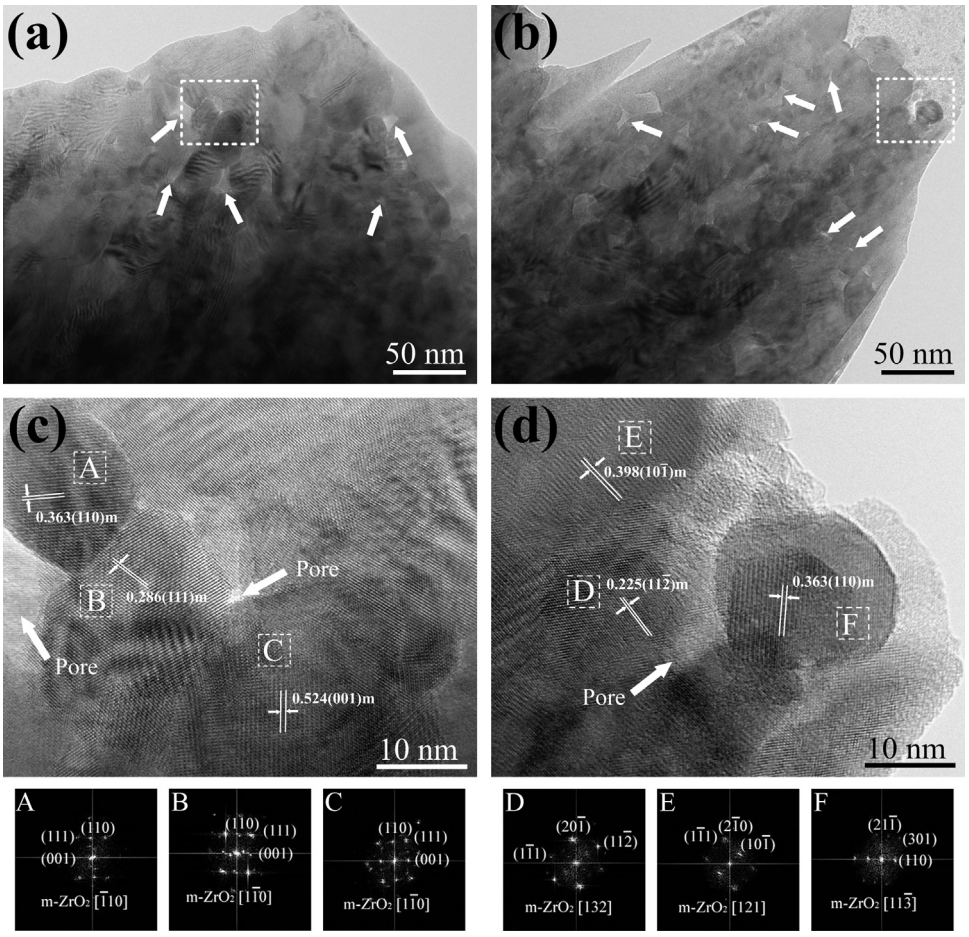

Fig. 7. TEM bright field micrographs on the outer oxide layer for (a) ZrNbFeO and (b) ZrNbFeSiO at 100 days exposure in LiOH aqueous. (c) and (d) HRTEM images for the square region marked in (a) and (b), respectively. The FFT diffraction patterns in the bottom are for the square regions A–F marked in (c) and (d).

listed in Table 4. According to the EDS results, both SPPs shown in Fig. 8 are partially oxidized. As represented in Fig. 8a and b, cracks paralleling to the interface form near the SPPs, as indicated by red arrows. A large-sized crack in the oxide of ZrNbFeO at 100 days of exposure in LiOH aqueous is found in Fig. 9, also about 0.5 μm from the interface. The crack propagates in a transgranular manner and is perpendicular to the growth direction of columnar grains (parallel to the interface). This crack is about 300 nm in length and across a few grains without correlating with any SPPs.

3.6. Tetragonal phase fraction analysis

Fig. 10 illustrates the calculated tetragonal phase fraction and the corresponding tetragonal phase amount from 100 days to 200 days exposure in deionized water (Fig. 10a and b) and LiOH aqueous solution (Fig. 10c and d), respectively. The corresponding tetragonal phase amount was calculated by normalizing the calculated tetragonal phase fraction with the corrosion weight gain of measured sample. With the continuous growth of the oxide, the fraction of tetragonal phase decreases at both corrosion conditions. The tetragonal phase fraction of ZrNbFeSiO is equivalent to or slightly higher than that of ZrNbFeO before transition, but it is considerably different from that of ZrNbFeO after transition (Fig. 10a and c). The absolute tetragonal oxide amount of ZrNbFeSiO is also a slightly higher than that of ZrNbFeO (Fig. 10b and d). A decrease in absolute tetragonal oxide amount is observed when the corrosion kinetics transition has occurred. The absolute tetragonal oxide amount of ZrNbFeO has a moderate growth after transition rather than being unchanged or decreasing (Fig. 10d). This augment in absolute tetragonal oxide amount also has been observed at the early stage of corrosion as reported in Ref. [10].

Table 4
Compositions of the precipitates quantified by the EDS analysis.

Precipitate	Element (at.%)				
	O	Si	Nb	Fe	Zr
A	27.83	–	18.19	20.25	31.19
B	30.17	0.93	19.22	17.41	32.27

4. Discussion

4.1. Effect of alloyed a trace of Si on microstructure and tensile properties

The dispersing second phase particles can refine the grains and inhibit the movement of dislocations and grain boundaries, thereby enhancing the strength and the recrystallization temperature [33,34]. Compared to ZrNbFeO, the main feature of microstructure of ZrNbFeSiO is partial recrystallization with finer precipitates (Fig. 3b). As shown in Table 2, the volume fractions of SPPs (3.29% for ZrNbFeO and 3.23% for ZrNbFeSiO) are nearly the same in both alloys. The size of SPPs in ZrNbFeSiO (55 nm) is smaller than that in ZrNbFeO (71 nm). Therefore, much more SPPs are presented in ZrNbFeSiO. Hong et al. [26] micro-alloyed Si to Zircaloy-4 and found the size of SPPs was finer than that in Si-free samples. As such, it

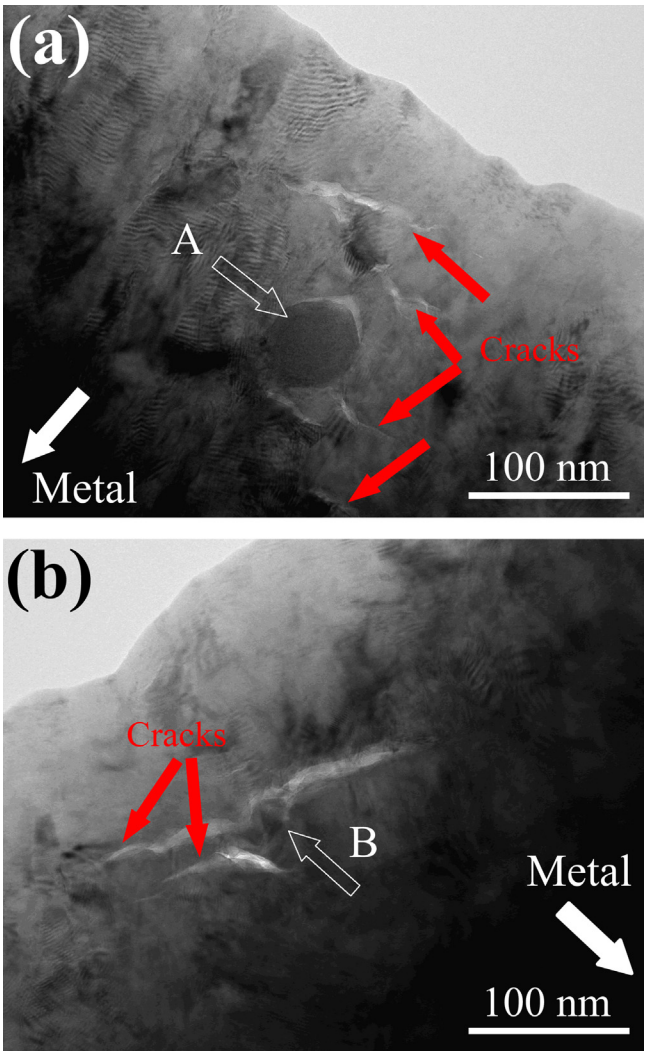

Fig. 8. TEM micrographs of second phase particles associated with cracks in the oxide of (a) ZrNbFeO and (b) ZrNbFeSiO at 100 days' exposure in LiOH aqueous, about 0.5 μm away from the interface.

is proposed that Si may play a role in phase nucleation during heat treatment and results in a refinement of precipitates. Herb et al. [35] investigated the precipitates growth in zirconium alloys during the manufacturing process and they found the Si-containing particles (~15 wt.% Si) have sluggish kinetics and grow at a rate of about 0.2 times slower than the Laves phase $Zr(Fe, Cr)_2$. It is reasonable that more SPPs exist in ZrNbFeSiO. The pinning effect of SPPs on grain boundaries and dislocations would be also stronger than those in ZrNbFeO due to much more SPPs existing in ZrNbFeSiO. Consequently, the degree of recrystallization of ZrNbFeSiO is much lower than that of ZrNbFeO. By coupling with effect low recrystallization and the dislocation cells observed in the Fig. 3d, ZrNbFeSiO exhibits higher strength and larger plasticity than ZrNbFeO.

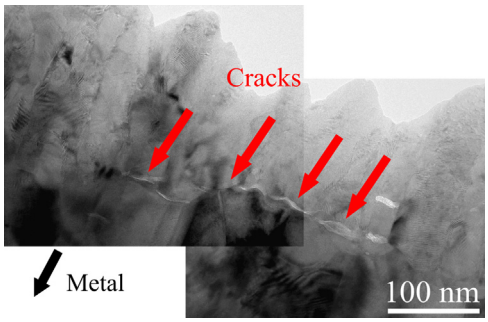

Fig. 9. TEM micrograph of long-sized crack in the oxide of ZrNbFeO at 100 days' exposure in LiOH aqueous, about 0.5 μm from the interface.

4.2. Role of alloyed Si in the oxide

Along with the effect of alloyed Si mentioned in the Section Introduction, the effect of Si on the corrosion might be much more complicated than what we expected. There are lots of intrinsic point defects existing in zirconia, such as vacancies and interstitial atoms [36]. Both experiments and calculations through density function theory have demonstrated that oxygen vacancies in zirconia can trap electrons from Si to form F centers (neutral oxygen vacancies) [36]. It has been reported that Si has a band gap smaller than that of monoclinic zirconia and oxygen vacancies can trap electrons from the conduction band of Si [37]. Therefore, a plausible mechanism for the effect of Si on corrosion resistance is suggested as followed. The charged oxygen vacancies become uncharged by trapping electron from Si. As the activation energy of diffusion for charged vacancies is much higher than that of uncharged vacancies [38], the mobility of vacancies decreases. As known, ion conductivity in zirconia is mediated via oxygen vacancies [38]. The decrease in the mobility of vacancies can reduce the mobility of oxygen ions

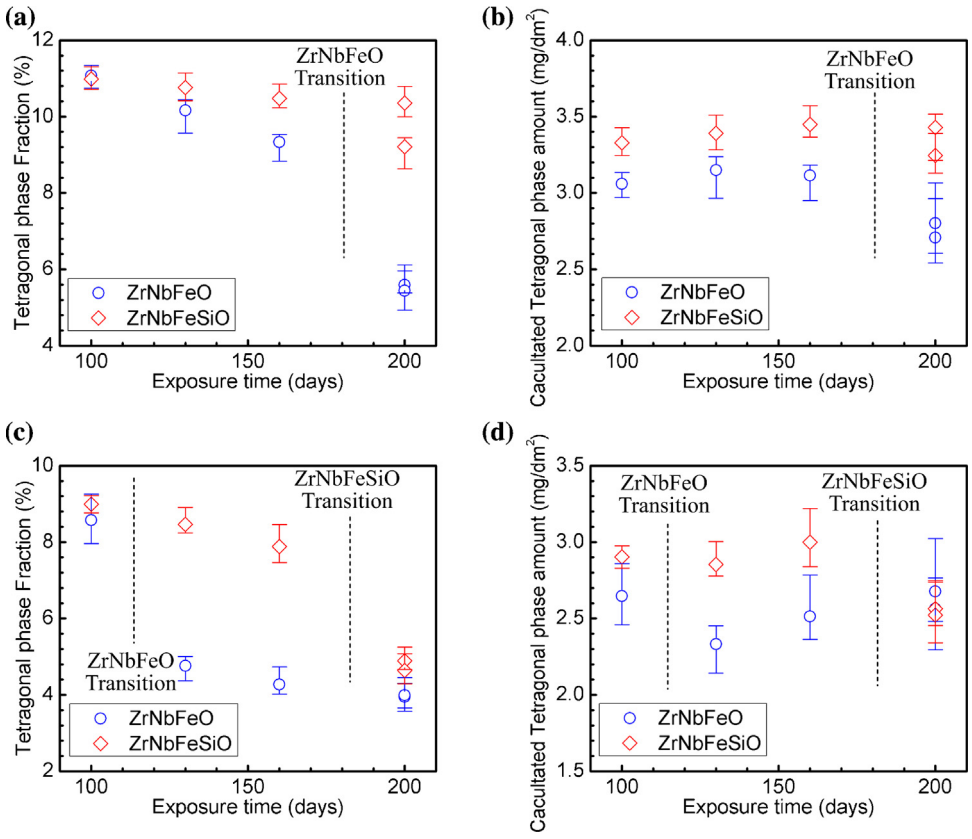

Fig. 10. Calculated phase fraction and the corresponding tetragonal phase amount plotted as a function of exposure time from 100 days to 200 days measured in (a) and (b) deionized water and (c) and (d) LiOH aqueous.

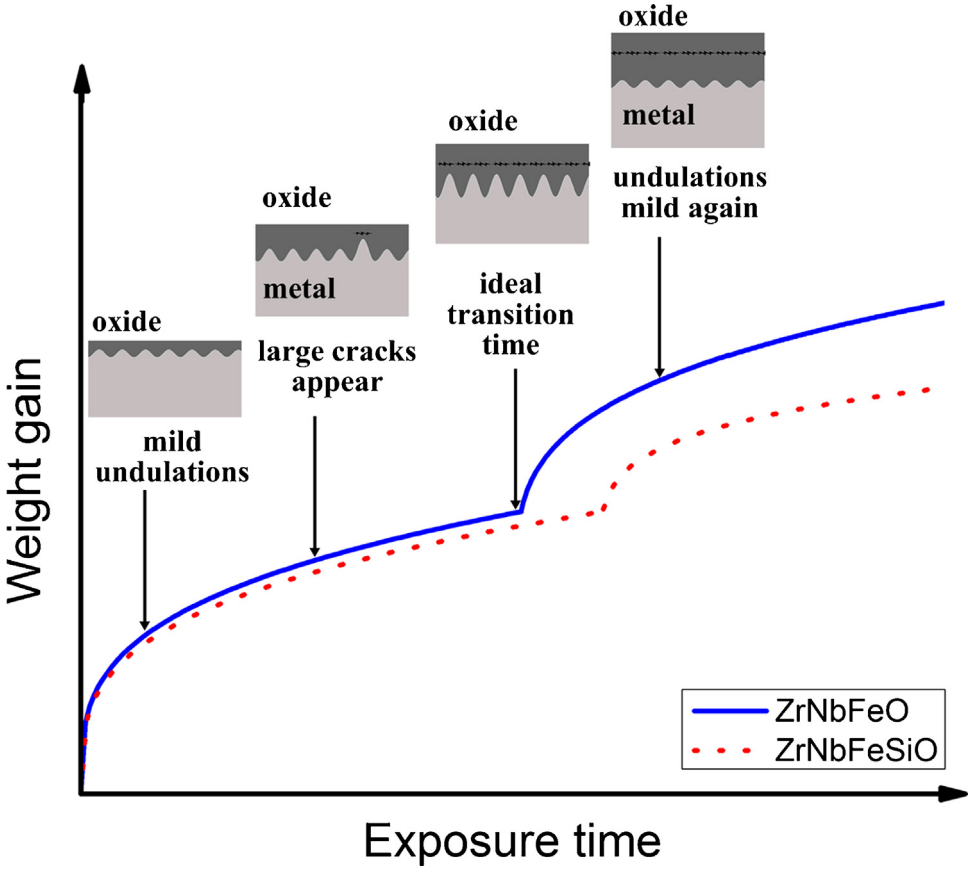

Fig. 11. Schematic illustration of the evolution of undutions and cracks during oxidation.

to some extent. Furthermore, due to the low solubility of Si in α-Zr [26], it is expected that almost all Si exists in SPPs. During corrosion, SPPs are incorporated into oxide and start to be oxidized when oxygen partial pressure is high enough. The element which has low electronegativity is expected to be oxidized first [16,39]. The electronegativity of Zr, Nb and Fe is 1.33, 1.59 and 1.83, respectively, which are lower than the electronegativity of Si(1.90) [39]. Thus, Si would be oxidized later than other elements in SPPs. Meanwhile, the oxidation of SPPs leads to volume dilation which induces internal stress and thus may increase the possibility of cracking in oxide [3,17]. The Pilling-bedworth (Pb) ratio of Zr, Nb and Fe is 1.56, 2.56, and 1.77, respectively, whilst the Pb ratio of Si is 2 and in the middle of other elements in SPPs [9]. It is more likely that the volume expansion of $(Zr, Nb, Si)_2Fe$ is not much different from that of $(Zr, Nb)_2Fe$. Actually, the content of Si in SPPs (less than 2.0 wt.%) is too low to substantially affect the action of SPPs during corrosion at both corrosion rate and/or volume dilation. That is, a trace of Si has little influence on stress alteration in oxide. Therefore, one can note that a trace of Si is more likely not to augment or slow the cracking by comparing the distribution of data in Fig. 5, as no specific crack in ZrNbFeSiO is observed. As discussed above, a trace of alloyed Si would not modify the susceptibility of oxide at a noticeable extent. Thus, the different evolution of oxides on both alloys might be attributed to the other factors, such as the undulations of the interface or the properties of the matrix.

4.3. The slow evolution of the undulated interface in ZrNbFeSiO

Although both alloys are still in the pre-transition and their weight gains are approximately same ($\approx 30\,mg\,dm^{-2}$) at 100 days exposure in LiOH aqueous solution (Fig. 1b and d), the undulations of interface in both alloys are extremely different (Fig. 4a and b). The evolution of undulations in ZrNbFeSiO is much slower than that in ZrNbFeO before transition. During oxide growth, mechanical stress is produced at the oxide/metal interface because of a significant difference in the specific volumes of the oxide and the metal as mentioned earlier [10,13,40]. The process that decreases mechanical energy is converting the oxide/metal interface to undulated state [12,13]. The level of this tensile stress will probably be limited only by the yield stress of the alloy [13].

A method of energy minimization to describe the evolution of undulations has been suggested by Likhanskii et al. [13]. When oxide formed adheres to the surface of the zirconium and is subjected to compressive stress, the formation of undulations could diminish the compressive energy in oxide, whilst the bending energy of oxide and deformation energy of metal increase simultaneously. It is assumed in the Ref. [13] that the interface of oxide and metal matrix is planar and the thickness of the oxide film is constant at the initial corrosion stage. Mechanical energy of both the oxide and metal increases while the oxide film grows on. Therefore, the relationship of amplitude a and mechanical energy ΔU can be given as [13]:

$$\Delta U = -\frac{(ka)^2}{8\epsilon}\frac{hE_{ox}}{1-\nu^2}\left[\frac{2(\epsilon-1)}{\epsilon}-\frac{(ka)^2}{4\epsilon}\right] + \frac{E_{ox}(kh)^3ka^2}{48\left(1-\nu^2\right)}\beta + \frac{1}{2}\sigma_{cr}\left[a-\sigma_{cr}\frac{\left(1-\nu_m^2\right)}{kE_m}\right] \quad (2)$$

where k is wave number, the amplitude is a and the oxide thickness is h, E_{ox} is the Young's modulus of oxide, E_m is the Young's modulus of metal, ν and ν_m are Poisson ratios for oxide and metal, ϵ is the coefficient of linear expansion during corrosion in plane of the interface, σ_{cr} is the yield strength of alloys, β could be considered as the bond strength between the grains in the oxide. The first term on the right hand of Eq. (2) depicts the decrease in elastic energy of the oxide film due to the increase in its length during formation of undulation. The second term on the right hand of Eq. (2) represents the bending strain energy in the oxide film. The third term and the forth term on the right hand of Eq. (2) describe the elastic stress energy and plastic deformation energy in metal substrate, respectively.

If the development of undulations is energetically favorable, its spontaneous formation is possible. It is found in calculations [13,40] that the formation of undulations is harder if the metal is at higher yield stress since more energy is needed. It should be noted that ZrNbFeSiO alloy has a higher yield strength than ZrNbFeO (Fig. 2). It is more difficult to acquire the same degree of deformation in ZrNbFeSiO. In other words, it implies that, in order to obtain the same undulation amplitude, more mechanical energy is needed in the alloy which has a higher yield strength. When the oxide becomes thicker, namely longer time exposure for corrosion, the oxide/metal interface in high yield strength zirconium alloy could get the equal undulation amplitude (Fig. 4d) comparable to that of the low yield strength zirconium alloy (Fig. 4a). Therefore, the smaller undulation amplitude is found in ZrNbFeSiO (Fig. 4b) compared to that in ZrNbFeO (Fig. 4a) at the same time exposure before transition.

4.4. The generation of cracks in oxide

The formation of undulations results in local stress redistribution in the oxide causing tensile stress above the wave crests [41,42]. This kind of tensile stress is perpendicular to the interface [10,41]. It is a prerequisite for the formation of cracks. Then the cracks which are parallel to the interface may present at the "weak" connection of oxide, such as flaw, microcrack or SPPs when the tensile stress is high enough [4]. As observed in this study, more cracks are associated with the sample which has low corrosion resistance. From the analysis of Fig. 5, no apparently visible crack is observed when the amplitude is less than 109 nm, indicating that it is a threshold of undulation amplitude for cracking and the shallow undulation may be too small to trigger a crack in the oxide. Vermaak et al. [10] computed the tensile stress above mild undulation which is only a fraction of that above sharp undulation and found that even such a high tensile stress could not reach the threshold for cracking. Therefore, the cracks in the oxide of ZrNbFeO are presented earlier than that of ZrNbFeSiO before transition (Fig. 4a and b).

In order to form a crack, not only a driving force in the form of a tensile stress is needed, but also a nucleation site is required. Cracks associated with SPPs are observed in Fig. 8 in both alloys. The SPPs are partially oxidized with cracks nearby (Table 4). It is hard to demonstrate whether the cracks form before oxidation of the SPPs. At least, the regions near SPPs are unstable and susceptible to cracking in both alloys. It was suggested that more SPPs would result in the formation of more cracks in oxide [15], which is however not observed at present work. Hence, the SPPs are not the sole reason for cracking. As exhibited in Fig. 9, a long-sized crack is across several columnar grains without associating with SPPs, indicating the other factor could also lead to formation of cracks. It is commonly accepted that the metastable tetragonal ZrO_2 phase could be stabilized at room temperature mainly by compressive stresses or small grain size in oxide [43]. As corrosion proceeding, compressive stresses in the oxide are gradually relaxed from the oxide/metal interface to the outer oxides [44]. This relaxation eventually results in an increased level of phase transformation (Fig. 10a and c). The continued transformation of t → m phase induces volume dilation and generates a lot of susceptible regions in the oxide, which it is believed to increase the possibility of cracking [17].

4.5. Periodic corrosion kinetics

With the results presented, the microstructural evolution and corrosion mechanism in the oxides are thus outlined and detailed corrosion process associated with the evolution of oxide can be schematically illustrated in Fig. 11. At the initiation of corrosion, both alloys have a very similar weight gain (Fig. 1). Firstly, there are the tight columnar grains with mildest undulations in the oxide without cracks (Fig. 6). It is convinced that the oxide is protective in this morphology [43]. According to the viewpoints discussed above, the evolution of undulations is determined by the mechanical energy which increases in both the oxide and the metal substrate when the oxide becomes thick. To decrease the mechanical energy in oxide/metal interface, the amplitude of undulations gets sharp. It is important to mention that the evolution of undulations is associated with the deformation of metal substrate. Under the condition of uniform oxide formed on both alloys, the alloy with high yield strength (ZrNbFeSiO) would have a slower evolution of the undulated interface than the alloy with low yield strength (ZrNbFeO).

As the corrosion proceeding as well as the mechanical stress accumulated in oxide/metal interface, the cracks are presented mostly above the sharp undulations (Fig. 4a and d) which reach a threshold as exhibited in Fig. 5. And with further deformation in the metal, more and more cracks are presented above all undulations. Both the SPPs and the transformation of t → m phase produce susceptible regions during corrosion proceeding. Until large cracks connect to each other and split the oxide into two layers (Fig. 4c), in this way much mechanical stress is relaxed without contributing to the development of undulations and thus the tetragonal phase has a sharp drop in absolute amount (Fig. 10b and d). These oxide layers have been reported previously by Yilmazbayhan et al. [45]. It was suggested that the oxide layers are correlated to the number of transitions in oxide growth. From the analysis of Ni et al. [32], one can speculate that the penetration of external oxidizing medium down to the linked-up cracks due to the porosity of the outer oxide layer (Fig. 7). Therefore, it is accompanied by a rapid increasing in corrosion rate since the thickness of protective oxide is reduced. In general, this process is considered as the corrosion kinetic transition. Therefore, the period of pre-transition is substantially extended in the alloy which has slower evolution of undulated interface, such as ZrNbFeSiO, and thus the corrosion resistance is enhanced.

The long link-up cracks split the oxide into two layers after the corrosion transition. The thickness of oxide which exerts strong compressive stress on metal substrate reduces and the mechanical energy on interface decreases correspondingly. The undulations develop to an energetically favorable state and become mild again (Fig. 4c). As the growth of inner oxide layer, it is expected that mechanical stress accumulated in oxide/metal interface once more, associated with the augment of the tetragonal phase in absolute amount (Fig. 10d) and the appearance of cracks above the sharp undulations. Polatidis et al. [30] also reported that the compressive stress for tetragonal phase has a shortly increase after transition. This tendency in compressive stress is in good agreement with the variations in the absolute tetragonal oxide amount observed in present work. Hence, multiple layered oxide and periodic corrosion kinetics are formed as well as in the other zirconium alloys, such as M5 and HANA6 [6,46], by this proposed mechanism.

5. Conclusions

A trace of alloyed Si in a Zr–Nb–Fe–O alloy refines second phase particles, decreases the degree of recrystallization, and enhances the strength of the alloy. However, a trace of alloyed Si does not deteriorate the nature of the oxide. Thus, the evolution of undulated interface which needs the deformation of metal substrate becomes slower. Consequently, the period of pre-transition of the alloy is extended and the corrosion resistance of the alloy is improved as well.

The evolution of undulations is associated with the appearance of cracks. Almost all cracks appear above the crests of undulations before transition. With the growth of oxide, more cracks are observed within oxide and the length of cracks augments with the increasing of amplitude of undulations. The corrosion kinetic transition occurs when the large cracks link up and split oxide into two layers. Meanwhile, tetragonal phase has a sharp drop in absolute amount, accompanying with a rapid increasing in corrosion rate. After the transition, the undulations of interface become mild again due to the thin oxide exert stress on metal substrate and few cracks is formed in the inner oxide layer.

Both the SPPs and the transformation of from tetragonal phase to monoclinic phase may provide susceptible regions for the formation of cracks. The driving force for cracking is the tensile stress which is perpendicular to the interface and stems from the local stress redistribution by the deformation of metal substrate. It is inevitably produced by the undulations of the interface. Therefore, this work advances the understanding of improving the corrosion resistance of zirconium alloys by enhancing the strength of alloy to slow down the evolution of undulations under the circumstance of ensuring the quality of oxide.

Acknowledgments

The authors would like to acknowledge a financial support provided by 973 Program under Grant No. 2014CB046701, National Science Foundation under Grant No. 51302168, Shanghai Natural Science Foundation under Grant No. 12ZR1445500, New Teachers' Fund for Doctor Stations, Ministry of Education under Grant No. 20120073120007, Shanghai Pujiang Program under Grant No. 15PJD017, Jiangxi Foreign Cooperation Program under Grant No. 20144BDH80004.

References

[1] Z.N. Yang, Y.Y. Xiao, F.C. Zhang, Z.G. Yan, Effect of cold rolling on microstructure and mechanical properties of pure Zr, Mater. Sci. Eng. A 556 (2012) 728–733.
[2] B. Panicaud, J.L. Grosseau-Poussard, D. Retraint, M. Guérain, L. Li, On the mechanical effects of a nanocrystallisation treatment for ZrO_2 oxide films growing on a zirconium alloy, Corros. Sci. 68 (2013) 263–274.
[3] J.Y. Park, B.-K. Choi, S.J. Yoo, Y.H. Jeong, Corrosion behavior and oxide properties of Zr-1.1 wt% Nb-0.05 wt% Cu alloy, J. Nucl. Mater. 359 (2006) 59–68.
[4] N. Ni, S. Lozano-Perez, J.M. Sykes, G.D.W. Smith, C.R.M. Grovenor, Focussed ion beam sectioning for the 3D characterisation of cracking in oxide scales formed on commercial ZIRLO™ alloys during corrosion in high temperature pressurised water, Corros. Sci. 53 (2011) 4073–4083.
[5] K. Takeda, H. Anada, Mechanism of corrosion rate degradation due to tin, zirconium in the nuclear industry, in: 12th International Symposium, ASTM STP 1354, 2000, pp. 592–608.
[6] J.Y. Park, B.K. Choi, S.J. Yoo, Y.H. Jeong, Corrosion and oxide properties of HANA alloys, J. ASTM Int. 5 (2008) 471–485.
[7] T. Arima, K. Miyata, Y. Inagaki, K. Idemitsu, Oxidation properties of Zr–Nb alloys at 500–600 °C under low oxygen potentials, Corros. Sci. 47 (2005) 435–446.
[8] L. Chen, J. Li, Y. Zhang, W. Lu, L. Zhang, L. Wang, D. Zhang, Effect of low temperature pre-deformation on precipitation behavior and microstructure of a Zr–Sn–Nb–Fe–Cu–O alloys during fabrication, J. Nucl. Sci. Technol. (2015), http://dx.doi.org/10.1080/00223131.2015.1059776 (in press).
[9] C. Xu, W. Gao, Pilling-Bedworth ratio for oxidation of alloys, Mat. Res. Innov. 3 (2000) 231–235.
[10] N. Vermaak, G. Parry, R. Estevez, Y. Bréchet, New insight into crack formation during corrosion of zirconium-based metal-oxide systems, Acta Mater. 61 (2013) 4374–4383.
[11] J. Wei, P. Frankel, E. Polatidis, M. Blat, A. Ambard, R.J. Comstock, et al., The effect of Sn on autoclave corrosion performance and corrosion mechanisms in Zr–Sn–Nb alloys, Acta Mater. 61 (2013) 4200–4214.

[12] J. Favergeon, T. Montesin, G. Bertrand, Mechano-chemical aspects of high temperature oxidation: a mesoscopic model applied to zirconium alloys, Oxid. Met. 64 (2005) 253–279.
[13] V.V. Likhanskii, T.N. Aliev, M.Y. Kolesnik, I.A. Evdokimov, V.G. Zborovskii, Method of elastic energy minimization for evaluation of transition parameters in oxidation kinetics of Zr alloys, Corros. Sci. 61 (2012) 143–147.
[14] P. Tejland, H.O. Andrén, Origin and effect of lateral cracks in oxide scales formed on zirconium alloys, J. Nucl. Mater. 430 (2012) 64–71.
[15] C. Proff, S. Abolhassani, C. Lemaignan, Oxidation behaviour of zirconium alloys and their precipitates—a mechanistic study, J. Nucl. Mater. 432 (2013) 222–238.
[16] W. Gong, H. Zhang, C. Wu, H. Tian, X. Wang, The role of alloying elements in the initiation of nanoscale porosity in oxide films formed on zirconium alloys, Corros. Sci. 77 (2013) 391–396.
[17] W. Qin, C. Nam, H.L. Li, J.A. Szpunar, Tetragonal phase stability in ZrO_2 film formed on zirconium alloys and its effects on corrosion resistance, Acta Mater. 55 (2007) 1695–1701.
[18] B. Cox, V.G. Kritsky, C. Lemaignan, V. Polley, I.G. Ritchie, H. Ruhmann, V.N. Shishov, Y.K. Bibilashvili, A.V. Nikulina, Waterside Corrosion of Zirconium Alloys in Nuclear Power Plants, International Atomic Energy Agency, 996, IAEA TECDOC, Vienna, 1998, pp. 124–169.
[19] Y.B. Chun, S.K. Hwang, S.I. Kwun, M.H. Kim, Abnormal grain growth of Zr-1 wt.% Nb alloy and the effect of Mo addition, Scr. Mater. 40 (1999) 1165–1170.
[20] J.H. Lee, S.K. Hwang, K. Yasuda, C. Kinoshita, Effect of molybdenum on electron radiation damage of Zr-base alloys, J. Nucl. Mater. 289 (2001) 334–337.
[21] K.I. Chang, S.I. Hong, Effect of sulphur on the strengthening of a Zr–Nb alloy, J. Nucl. Mater. 373 (2008) 16–21.
[22] Y.C. Choi, S. Ko, K.I. Chang, N.C. Cho, S.I. Hong, Effect of phosphorus on the mechanical behavior of a Zr–Nb alloy, J. Nucl. Mater. 383 (2009) 270–273.
[23] A.A. Arie, W. Chang, J.K. Lee, Electrochemical characteristics of semi conductive silicon anode for lithium polymer batteries, J. Electroceram. 24 (2010) 308–312.
[24] J.W. Boldeman, B.J. Allen, A.L. de, R.L.M. Musgrove, The neutron capture cross section of natural silicon, Nucl. Phys. A 252 (1975) 62–76.
[25] S. Jin, C. Leinenbach, J. Wang, L.I. Duarte, S. Delsante, G. Borzone, et al., Thermodynamic study and re-assessment of the Ge–Ni system, Calphad 38 (2012) 23–34.
[26] H.S. Hong, S.J. Kim, K.S. Lee, Influence of dilute silicon addition on the oxidation resistance and tensile properties of modified Zircaloy-4, J. Nucl. Mater. 304 (2002) 8–14.
[27] L. Chen, J. Li, Y. Zhang, L.C. Zhang, W. Lu, L. Wang, Zr–Sn–Nb–Fe–Si–O alloy for fuel cladding candidate: processing, microstructure, corrosion resistance and tensile behavior, Corros. Sci. 100 (2015) 332–340.
[28] R.C. Garvie, P.S. Nicholson, Phase analysis in zirconia systems, J. Am. Ceram. Soc. 55 (1972) 303–305.
[29] A. Ly, A. Ambard, M. Blat-Yrieix, L. Legras, P. Frankel, M. Preuss, Understanding crack formation at the metal/oxide interface during corrosion of Zircaloy-4 using a simple mechanical model, J. ASTM Int. 8 (2011) 1–29.
[30] E. Polatidis, P. Frankel, J. Wei, M. Klaus, R.J. Comstock, A. Ambard, et al., Residual stresses and tetragonal phase fraction characterisation of corrosion tested Zircaloy-4 using energy dispersive synchrotron X-ray diffraction, J. Nucl. Mater. 432 (2013) 102–112.
[31] S.D. Antolovich, R.W. Armstrong, Plastic strain localization in metals: origins and consequences, Prog. Mater. Sci. 59 (2014) 1–160.
[32] N. Ni, D. Hudson, J. Wei, P. Wang, S. Lozano-Perez, G.D.W. Smith, et al., How the crystallography and nanoscale chemistry of the metal/oxide interface develops during the aqueous oxidation of zirconium cladding alloys, Acta Mater. 60 (2012) 7132–7149.
[33] D.B. Williams, E.P. Butler, Grain boundary discontinuous precipitation reactions, Int. Met. Rev. 26 (1981) 153–183.
[34] L.H. Su, C. Lu, L.Z. He, L.C. Zhang, P. Guagliardo, A.K. Tieu, et al., Study of vacancy-type defects by positron annihilation in ultrafine-grained aluminum severely deformed at room and cryogenic temperatures, Acta Mater. 60 (2012) 4218–4228.
[35] H. Herb, In-process investigation of precipitate growth in zirconium alloys, zirconium in the nuclear industry, in: 12th International Symposium, ASTM STP 1354, 2000, pp. 482–504.
[36] M. Youssef, B. Yildiz, Intrinsic point-defect equilibria in tetragonal ZrO_2: density functional theory analysis with finite-temperature effects, Phys. Rev. B. 86 (2012) 144109.
[37] A.S. Foster, V.B. Sulimov, F.L. Gejo, A.L. Shluger, R.M. Nieminen, Structure and electrical levels of point defects in monoclinic zirconia, Phys. Rev. B 64 (2001) 224108.
[38] A. Eichler, Tetragonal Y-doped zirconia: structure and ion conductivity, Phys. Rev. B 64 (2001) 174103.
[39] K. Ohwada, On the pauling electronegativity scales—II, Polyhedron 3 (1984) 853–859.
[40] V. Likhanskii, M. Kolesnik, On the evolution of wave structure at the metal/oxide interface during oxidation of Zr alloys, Corros. Sci. 87 (2014) 416–420.
[41] M. Parise, O. Sicardy, G. Cailletaud, Modelling of the mechanical behavior of the metal–oxide system during Zr alloy oxidation, J. Nucl. Mater. 256 (1998) 35–46.
[42] M. Parise, R. Foerch, G. Cailletaud, Coupling between diffusion and mechanics during the oxidation of zircaloy, J. Phys. IV 9.9 (1999) 311–320.
[43] W. Gong, H. Zhang, Y. Qiao, H. Tian, X. Ni, Z. Li, et al., Grain morphology and crystal structure of pre-transition oxides formed on Zircaloy-4, Corros. Sci. 74 (2013) 323–331.
[44] B. Griggs, H.P. Maffei, D.W. Shannon, Multiple rate transitions in the aqueous corrosion of zircaloy, J. Electrochem. Soc. 109 (1962) 665–668.
[45] A. Yilmazbayhan, E. Breval, A.T. Motta, R.J. Comstock, Transmission electron microscopy examination of oxide layers formed on Zr alloys, J. Nucl. Mater. 349 (2006) 265–281.
[46] P. Bossis, D. Pecheur, L. Hanifi, J. Thomazet, M. Blat, Comparison of the high burn-up corrosion on M5 and low tin Zircaloy-4, J. ASTM Int. 3 (2006) 494–525.